Intermediate spin state and the *B*1-*B*2 transition in ferropericlase

Tianqi Wan [1], Yang Sun [1], and Renata M. Wentzcovitch [1,2,3,*]

[1]*Department of Applied Physics and Applied Mathematics, Columbia University, New York, New York 10027, USA*
[2]*Department of Earth and Environmental Sciences, Columbia University, New York, New York 10027, USA*
[3]*Lamont-Doherty Earth Observatory, Columbia University, Palisades, New York 10964, USA*

Ferropericlase (*fp*), $(Mg_{1-x}Fe_x)O$, the second most abundant mineral in the Earth's lower mantle, is expected to be an essential component of the mantles of super-Earths. Here, we present an *ab initio* investigation of the structure and magnetic ground state of *fp* up to ~ 3 TPa with iron concentrations (x_{Fe}) varying from 0.03 to 0.12. Calculations were performed using LDA $+ U_{sc}$ and PBE exchange-correlation functionals to elucidate the pressure range for which the Hubbard U (U_{sc}) is required. Similar to the end members FeO and MgO, *fp* also undergoes a *B*1-to-*B*2 phase transition that should be essential for modeling the structure and dynamics of the mantles of super-Earths. This structural transition involves a simultaneous change in magnetic state from a low-spin (LS) *B*1 phase with iron total spin $S = 0$ to an intermediate-spin (IS) *B*2 phase with $S = 1$. This is a rare form of pressure/strain-induced magnetism produced by local cation coordination changes. Phonon calculations confirm the dynamical stability of the iron *B*2-IS state. Free energy calculations are then carried out including vibrational effects and electronic and magnetic entropy contributions. The phase diagram is then obtained for low-concentration *fp* using a quasi-ideal solid solution model. For $x_{Fe} > 0.12$, this approach is no longer valid. At ultrahigh pressures, there is an IS-to-LS spin state change in Fe in the *B*2 phase, but the transition pressure depends sensitively on thermal electronic excitations and on x_{Fe}.

I. INTRODUCTION

Ferropericlase (*fp*), i.e., rocksalt-type $(Mg_{1-x}Fe_x)O$ ($x_{Fe} < 0.5$) is a major phase of the Earth's lower mantle defined by the 660 km discontinuity produced by the postspinel transition [1]. Based on the expected composition of rocky exoplanets [2], it is also expected to exist in the mantles of super-Earths [3,4], i.e., planets with up to ~ 14 Earth masses ($M_\oplus$). These planets are relevant in searching for habitable planets and extraterrestrial life; therefore, there is great interest in understanding their internal structure and geophysical properties. Considerable effort is dedicated to discovering their constituent phases and their properties. Such phases are primarily silicates, oxides, and iron alloys involving Mg, Al, Ca, Fe, Si, H, S, and C. The first step has been to assume compositions close to Earth's and those of other terrestrial solar planets [2] and add complexity as knowledge advances.

The properties of *fp* are well studied within the Earth pressure range. For instance, iron in *fp* undergoes a spin-state change from a high spin (HS) with total spin $S = 2$ to a low spin (LS) with $S = 0$ [5,6]. However, on Earth, pressure and temperature at the core-mantle boundary (CMB)

are only 0.135 TPa and ~ 4000 K. At this condition, *fp* can still maintain NaCl-type (*B*1) structure [7]. In some terrestrial exoplanets, CMB conditions might reach several TPa and $\sim 10\,000$ K [4]. At ~ 600 GPa, MgO undergoes a transition from the *B*1 (NaCl-type) to the *B*2 (CsCl-type) [8,9], which is also expected in *fp* at ultrahigh pressures [10]. A considerable viscosity reduction across this transition has been reported, which may have great impact on the mantle convection in super-Earths [11]. To better understand terrestrial mantles and the behavior of iron in related phases, characterization of *fp* in a broader range of pressure and temperature conditions has gained interest in the last few years [12,13]. However, the complexity of the structural change coupled to a possible spin-state change in *fp* makes the *B*1 structural stability field largely unknown and challenging to pin down at ultrahigh temperatures and pressures.

The presence of localized $3d$ electrons in iron requires methods that go beyond standard density functional theory (DFT) to address their strongly correlated nature [14–19]. DFT $+ U$ is a popular method that adds the Hubbard correction to standard DFT calculations [19,20]. The reliability of DFT $+ U$ results depends greatly on the Hubbard parameter U. To be predictive, U should be determined by *ab initio* [15] self-consistently [21] and be structure- and spin-state dependent [22–27]. Moreover, electron delocalization under pressure induces an insulator-to-metal transition (IMT) in the FeO end member [28], and it should also occur in *fp* at some high pressure. Therefore, the performance of DFT $+ U$ and other functionals needs to be examined carefully and consistently in both metallic and insulating states of *fp*.

*Corresponding author: rmw2150@columbia.edu

We study the $B1$-$B2$ structural transition and iron spin states in fp up to 3 TPa using LDA + U_{sc} and conventional DFT methods. The dependence of U on pressure, volume, structure, and spin state are carefully considered in the $(Mg_{1-x}Fe_x)O$ system with x_{Fe} up to 0.125 at ultrahigh pressures and temperatures. Various entropic contributions have also been included in the free energy and phase diagram calculations.

This paper is organized as follows. In Sec. II, we present the details of computational methods. Section III offers an electronic structure analysis, including spin states, free energy calculations, and phase diagrams. Section IV presents our conclusions.

II. METHOD

A. *Ab initio* calculations

Ab initio calculations are carried out with the QUANTUM ESPRESSO code [29,30]. Local density approximation (LDA) and LDA + U_{sc} calculations use Vanderbilt's ultrasoft pseudopotentials [31] with valence electronic configurations $3s^2 3p^6 3d^{6.5} 4s^1 4p^0$ and $2s^2 2p^4$ for Fe and O, respectively. The pseudopotential for Mg was generated by the method of von Barth–Car using five configurations $3s^2 3p^0$, $3s^1 3p^1$, $3s^1 3p^{0.5} 3d^{0.5}$, $3s^1 3p^{0.5}$, and $3s^1 3d^1$ with decreasing weights 1.5, 0.6, 0.3, 0.3, and 0.2, respectively. These pseudopotentials for Fe, Mg, and O were generated, tested, and previously used, e.g., in Umemoto *et al.* [32]. Perdew-Burke-Ernzerhof (PBE) [33] calculations are carried out using the projector augmented wave (PAW) method with PAW dataset from the PSLIBRARY [34]. Plane-wave energy cutoffs are 100 and 1000 Ry for electronic wave functions and spin-charge density and potentials, respectively. The irreducible Brillouin zone of the 64-atom supercell is sampled by a $6 \times 6 \times 6$ Monkhorst-Pack mesh [35] when computing the charge density. Effects of larger energy cutoff and k-point sampling on calculated properties are insignificant. The convergence thresholds are 0.01 0.01 eV/Å for all components (f_x, f_y, and f_z) of all forces, including atomic forces and averaged forces in the supercell, and 1×10^{-6} eV for the total energy of the supercell, 64 atoms in this paper. The Mermin functional is used in all calculations [36,37], to address the important effect of thermal electronic excitation on the free energy and dynamical stability of the phases.

In LDA + U_{sc} calculations, the Hubbard correction [19] is applied to Fe-$3d$ states. The Hubbard parameter U is computed using density functional perturbation theory [38]. The convergence threshold for the response function is 1×10^{-6} eV. We employed an automated iterative scheme to obtain the self-consistent U_{sc} parameter while simultaneously optimizing the structure and spin state [25]. Starting from an empirical $U = 4.3$ eV, we compute energies corresponding to all possible occupation matrices for a particular spin state. The electronic configuration, i.e., occupation matrix with the lowest energy, is then selected to further structural optimization using variable cell shape molecular dynamics [39,40]. Then a new U parameter is recalculated for further structural optimization. The process continues until mutual convergence of structure and U is achieved [25] for a convergence threshold

of 0.01 eV for the U parameter and the convergence criteria mentioned above for structural optimizations. For the metallic states, we use the Mermin functional in calculations *a posteriori*, i.e., without further changing U from self-consistent calculations.

Phonon calculations are performed in 64-atom supercells using the finite-displacement method with the PHONOPY code [41] and LDA + U_{sc} forces obtained with the QUANTUM ESPRESSO. All phonon calculations used the Mermin functional [36,37,42]. Vibrational density of states are obtained using a q-point $6 \times 6 \times 6$ mesh. The vibrational contribution to the free energy is calculated using the quasiharmonic approximation [43].

B. Quasi-ideal solid solution model

We address the $B1$-$B2$ phase boundary using a binary solid solution model without computing the free energy of the FeO end member. The MgO-FeO system does not form an ideal solid solution (ISS). FeO-MgO interactions cannot be neglected, and we do not do so. Supercell calculations naturally include the MgO-FeO interaction energy, even using a single atomic configuration. For $x_{Fe} < 0.125$, iron atoms are well separated on average, and the energy difference between various supercell atomic configurations can be disregarded without significant effects. Fe atoms are surrounded by O, and Mg is most likely the second nearest neighbor (see structures in Fig. S5 in the Supplemental Material [44]). Given this situation, a single atomic configuration of fp with small x_{Fe} can be considered as an end member of a dilute solid solution. Therefore, instead of using the free energy of the FeO and MgO in the ISS modeling, one can calculate the free energy for some small x_B ($x_B < 0.125$ in this paper) using MgO and $(Mg_{0.875}Fe_{0.125})O$ as end members.

Specifically, in an A-B binary system (MgO-FeO in the current case) at a given pressure and temperature, the Gibbs free energy of mixing curves of $B1$ and $B2$ ISSs are

$$\Delta \mathcal{G}_{Mix}^{B1} = k_B T [x_B \ln x_B + (1 - x_B) \ln (1 - x_B)] + x_B (\Delta G_B^{B1-B2}), \tag{1a}$$

$$\Delta \mathcal{G}_{Mix}^{B2} = k_B T [x_B \ln x_B + (1 - x_B) \ln (1 - x_B)] - (1 - x_B)(\Delta G_A^{B1-B2}), \tag{1b}$$

with k_B as the Boltzmann constant and $x_B = x_{Fe}/0.125$, where x_{Fe} is the iron concentration. Here, ΔG_A^{B1-B2} and ΔG_B^{B1-B2} are the free energy differences of the end members in the two phases involved, i.e., $\Delta G_A^{B1-B2} = G_A^{B1} - G_A^{B2}$ and $\Delta G_B^{B1-B2} = G_B^{B1} - G_B^{B2}$. End member A corresponds to MgO, while end member B is $(Mg_{0.875}Fe_{0.125})O$. In this case, the ISS-like modeling includes interaction between the standard MgO-FeO end members. We refer to this level of modeling as a quasi-ISS (QISS; see Supplemental Material [44]) [45].

In a binary solid solution model, the compositions of the $B1$-$B2$ solvus lines are

$$X_B^{B2} = \frac{1 - \exp\left(-\frac{\Delta G_A^{B1-B2}}{k_B T}\right)}{\exp\left(-\frac{\Delta G_B^{B1-B2}}{k_B T}\right) - \exp\left(-\frac{\Delta G_A^{B1-B2}}{k_B T}\right)},$$
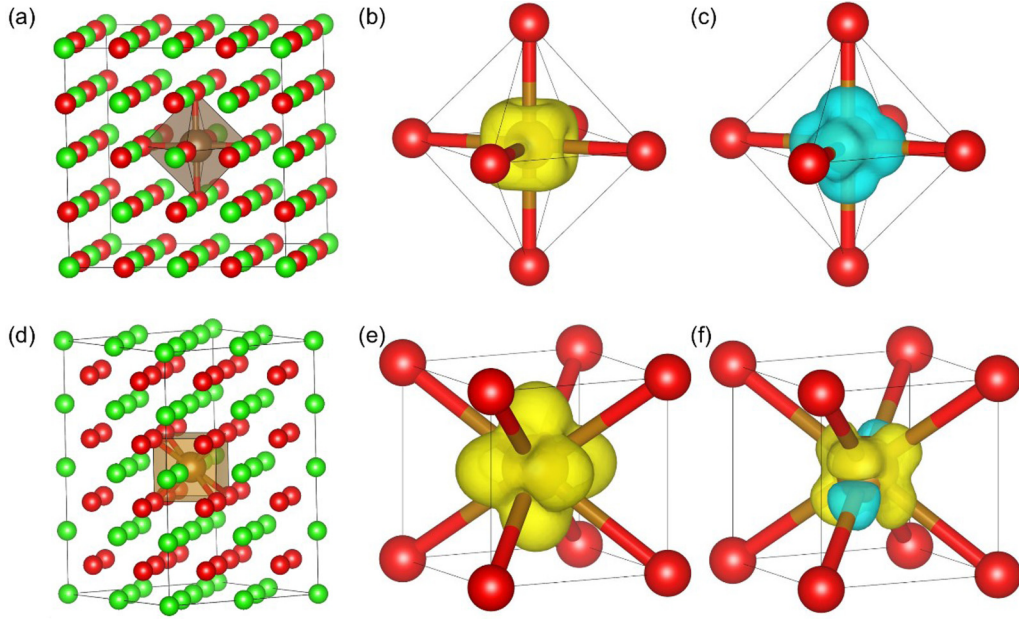
FIG. 1. Atomic structures of (a) *B*1 and (d) *B*2 phases with $x_{Fe} = 0.03125$; (b) fully occupied t_{2g} orbitals and (c) unoccupied e_g orbitals of low-spin (LS) Fe^{2+} in the octahedral crystal field of the *B*1 structure; (e) fully occupied e_g orbitals and (f) half occupied e'_g (formerly t_{2g}) of intermediate-spin (IS) Fe^{2+} in the cubic crystal field; yellow and blue represent occupied, fully or partially, and unoccupied orbitals, respectively. Green, brown, and red represent Mg, Fe, and O, respectively.

$$X_B^{B1} = X_B^{B2} \exp\left(-\frac{\Delta G_B^{B1-B2}}{k_B T}\right). \tag{1c}$$

The *B*2 mol fraction n_{B2} is given by the lever rule:

$$n_{B2} = \frac{x_B - X_B^{B1}}{X_B^{B2} - X_B^{B1}}. \tag{1d}$$

III. RESULTS

A. Intermediate spin state in the *B*2 structure

We first investigate the electronic structure, including the spin states, of $FeMg_{31}O_{32}$ ($x_{Fe} = 0.03125$, noted as *fp*3 hereafter), in the *B*1 and *B*2 phases. To create a similar 64-atom cell in the *B*2 phase, we constructed a $2\sqrt{2} \times 2\sqrt{2} \times 4$ supercell. The crystal structures are shown in Figs. 1(a) and 1(b).

According to several previous studies, the HS-LS static transition in the *B*1 phase occurs at ∼60 GPa in *fp*3 [46]. Therefore, in the pressure range considered here, i.e., 300 GPa to 2 TPa, *B*1 *fp* is in the LS state. However, the spin state of *fp* in the *B*2 structure is mainly unknown. Due to different cation coordination, the 3*d* energy level degeneracies in Fe^{2+} in the *B*2 and *B*1 structures differ. Fe^{2+} is octahedrally coordinated in the *B*1 phase, and the fivefold *d* levels split mainly into a lower triplet, the t_{2g} states, and an upper doublet, the e_g states with further smaller Jahn-Teller splitting. The e_g orbitals point toward negatively charged n.n. oxygens, while the t_{2g} orbitals point away from them [see Figs. 1(b) and 1(c)]. Electrostatic interaction contributes to lowering the energy of t_{2g} orbitals relative to those of e_g orbitals in the octahedral environment. In the *B*2 phase, Fe^{2+} has cubic coordination. The t_{2g} orbitals point to the n.n. oxygens, while the e_g orbitals point to the interstitial sites, away from them [see Figs. 1(e) and 1(f)].

Therefore, the doublet e_g becomes energetically favorable relative to the t_{2g} triplet in the *B*2 structure. Jahn-Teller splitting is also observed in this case.

The change in the electronic energy levels in going from the *B*1 to the *B*2 structure induces changes in the spin state and Fe-O bond lengths, i.e., Jahn-Teller distortions. In the *B*1 phase, Fe^{2+} exists in the HS and LS states with configurations $d_\uparrow^5 d_\downarrow^1$ and $d_\uparrow^3 d_\downarrow^3$, respectively. Two intermediate spin (IS) states, $d_\uparrow^4 d_\downarrow^2$, with different occupation matrices were shown to be metastable in Fe^{2+} in *B*1-type *fp*. In the *B*2 phase, the IS state can be stabilized due to the lower e_g doublet and an additional Jahn-Teller splitting in the t_{2g} triplet. In this state, four electrons occupy all e_g orbitals, and the remaining two electrons occupy two of the t_{2g} orbitals, now e'_g, producing a $d_\uparrow^4 d_\downarrow^2$ electronic configuration with $S = 1$. Therefore, the cubic crystal field favors the formation of the IS state. Alternatively, the two electrons in the e'_g manifold can occupy a single e'_g orbital, with spin up and down, producing the LS state with $d_\uparrow^3 d_\downarrow^3$. As shown later, the *B*2-LS state is metastable in the cubic crystal field at lower pressures.

Figure 2 shows t_{2g} and e_g projected density of states (PDOS) in the *B*2-IS phase ($d_\uparrow^4 d_\downarrow^2$). Figure 2(a) shows that the 3*d* electron PDOS of the clamped ion structure is metallic with an electronic (Mermin) temperature $T_{el} = 300$ K. The three t_{2g} up orbitals at the Fermi level are partially occupied with $\sim\frac{2}{3}$ occupancy. The FeO bond lengths in this state with cubic coordination are the same. In this situation, *fp*3 shows imaginary phonon frequencies pointing to structural instability. We add the displacement mode corresponding to the largest imaginary frequency to the undistorted structure and relax the atomic positions with $T_{el} = 300$ K. Figure 2(b) shows the resulting structure with shorter Fe-O bond lengths
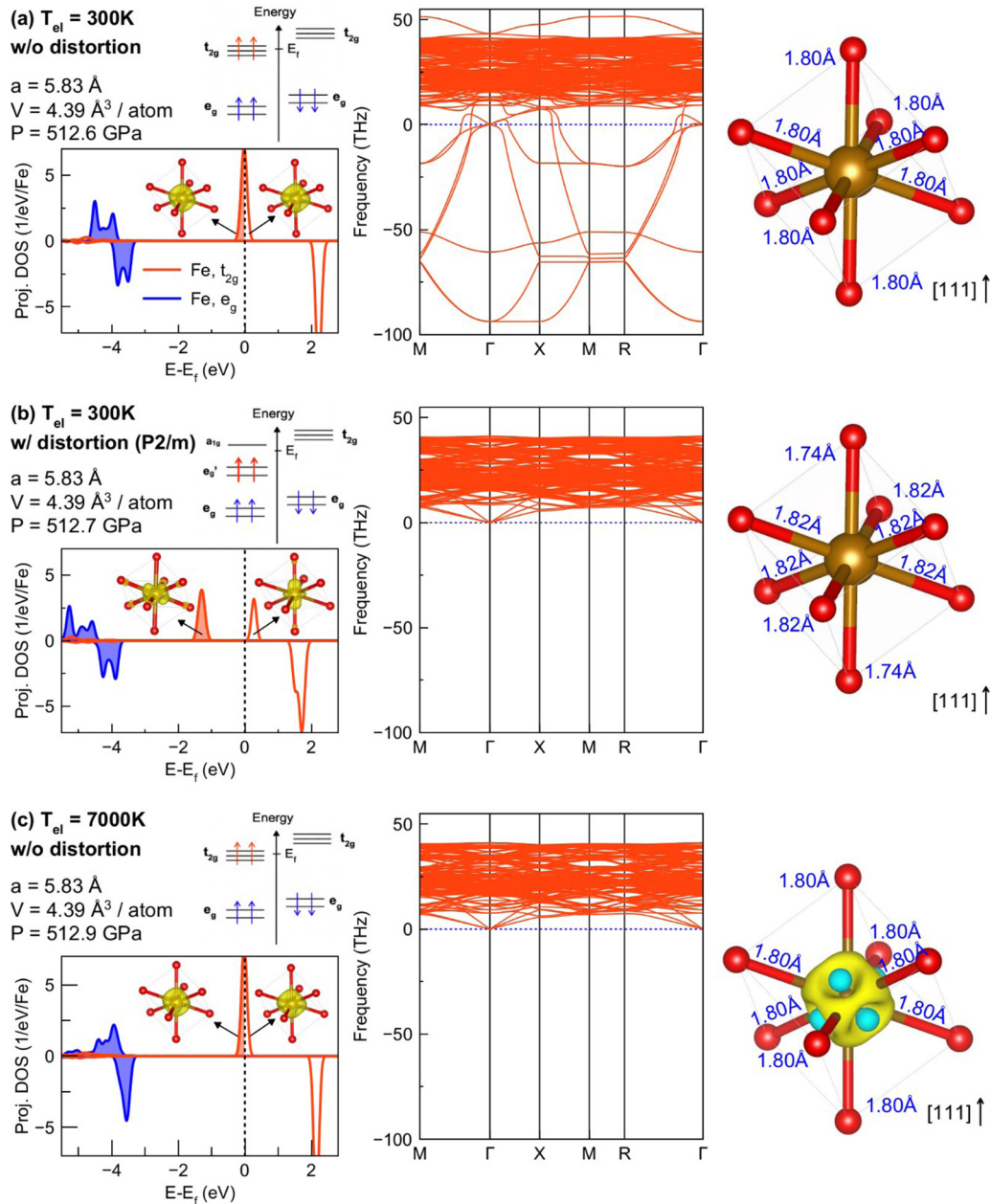
FIG. 2. Left panel: t_{2g} and e_g projected density of states (PDOS), charge density, and electron occupation diagram for the *3d* electrons in Fe^{2+} in the *B2*-intermediate-spin (IS) state for $x_{Fe} = 0.03125$ obtained with LDA + U_{sc}. Middle: Corresponding phonon dispersions. Right panel: Fe-O bond lengths and charge difference between (a) and (c). $\Delta\rho = \rho(7000\,K) - \rho(300\,K)$. The charge moves from blue to yellow regions.

along [111], i.e., a local rhombohedral distortion. The t_{2g} triplet splits into an a_{1g} singlet and an e'_g doublet with this distortion. With two electrons occupying the doublet, the system becomes insulating with a bandgap of 1 eV shown in Fig. 2(b). In contrast, with $T_{el} = 7000$ K, a more realistic temperature for exoplanetary interiors, the system is metallic again, and phonon instabilities are no longer present in the cubic environment [see Fig. 2(c)]. The right panel in Fig. 2(c) shows the charge distribution difference between the distorted structure [Fig. 2(b)] with $T_{el} = 300$ K and the cubic structures with $T_{el} = 7000$ K. We see a charge transfer from interstitial regions to the bonding region, which helps to delocalize the *d* electrons among the three t_{2g} states. Despite the finite carrier

concentration at the Fermi level, a disordered material with such a narrow electronic bandwidth may not behave as a conductor.

We note that the T_{el}-dependent phonon instability revealed in Fig. 2 does not depend on the functional or iron composition. Similar results are produced with the PBE functional and with $x_{Fe} = 0.125$ (see Figs. S1 and S2 in the Supplemental Material [44]). In all cases, the increasing T_{el} leads to a systematic increase of phonon stability (see also Figs. S3 and S4 in the Supplemental Material [44]). However, the uncertainty in the LDA + U_{sc} gap and electron-phonon and phonon-phonon interactions not addressed in this calculation naturally introduce uncertainty in the T_{el} necessary to remove
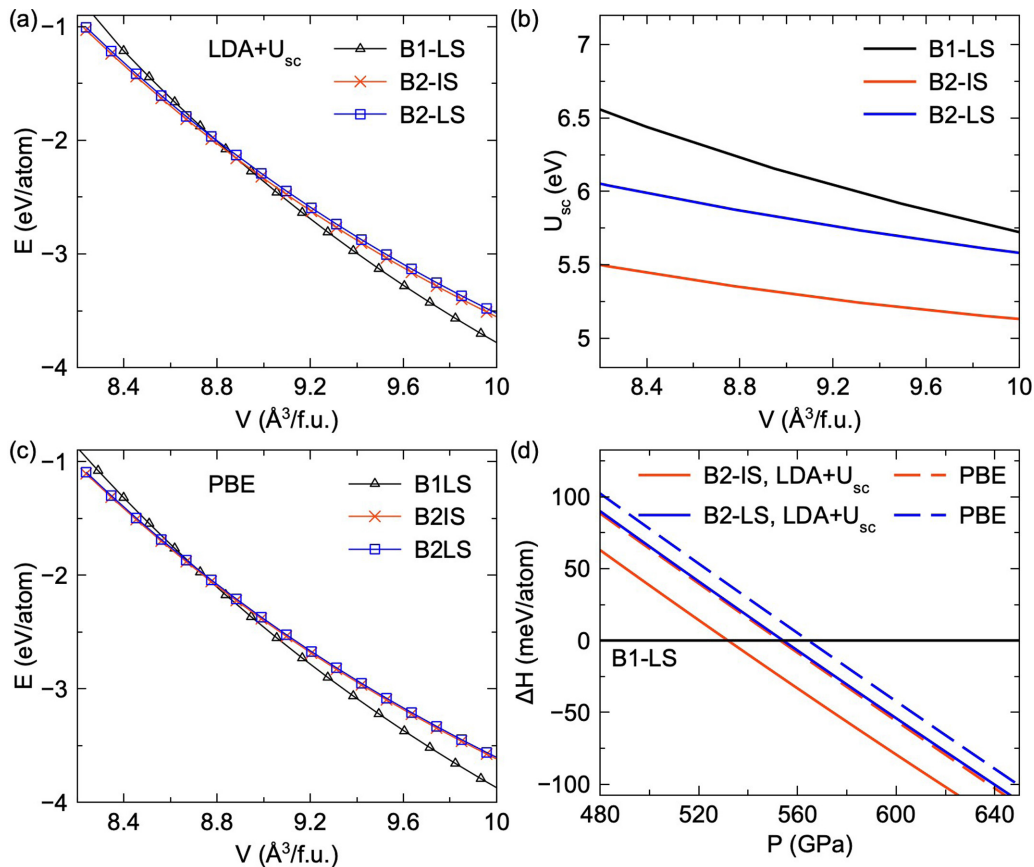
FIG. 3. (a) Energy-volume curves for *B*2-intermediate-spin (IS), *B*2-low-spin (LS), and *B*1-LS states with $x_{Fe} = 0.03125$. (a) LDA + U_{sc} calculations. (b) The self-consistent Hubbard parameters U. (c) PBE results. (d) Relative enthalpies using *B*1-LS as the reference.

the Jahn-Teller instability. In addition, *fp* must be a disordered solid solution at high temperatures; therefore, coherent rhombohedra distortions at low temperatures, as shown in Fig. 2(b), are less likely to form when Fe is randomly distributed.

B. *B*1-*B*2 phase transitions in *fp*3

To determine the relative stability of *B*1 and *B*2 phases in *fp*3, we perform LDA + U_{sc} and PBE calculations in a large volume (pressure) range with $T_{el} = 1000$ K. All atomic positions are fully optimized to accommodate favorable Jahn-Teller distortions. In the relaxed structures at ∼600 GPa, we find the average Fe-O bond lengths are longer than the Mg-O ones by 0.8% in the *B*2-IS state and 0.9% in the *B*2-LS state. Figure 3(a) shows the volume-dependent total energy of different states. Upon decreasing volume, the *B*1-LS state becomes less favored than the *B*2 states. Figure 3(b) shows the self-consistent and structurally consistent Hubbard parameters obtained in these calculations. The *B*2-IS state shows systematically lower U values than the LS states. This trend is like that seen in the U parameters in FeO where the LS state of Fe^{2+} always shows the largest self-consistent U value, regardless of crystal structure [25]. The U values of *B*1-LS and *B*2-LS differ by ∼1 eV. This shows the Hubbard parameter has a substantial volume and structure dependence in addition to the electronic configuration dependence. Figure 3(c) shows similar PBE results indicating a very similar *B*1-*B*2 transition behavior, with PBE transition pressures being higher by 10–30

GPa than LDA + U_{sc} transition pressures, a typical difference in performance between LDA and PBE functionals [47].

The energy vs volume results of each state is fit with the Birch-Murnaghan (BM) equation of state (EoS). Detailed EoS parameters are shown in Supplemental Material Tables S1 and S2 [44]. Enthalpies obtained from the static BM-EoS are shown in Fig. 3(d). Regardless of the functional, the *B*2-IS phase always shows lower enthalpy than the *B*2-LS in the pressure range considered here, indicating that the IS state is the ground state in the *B*2-type phase for small x_{Fe}. The static *B*1-LS → *B*2-IS transition pressure is 531 GPa in LDA + U_{sc} calculations and 554 GPa in PBE calculations.

C. *B*1-*B*2 phase boundary up to $x_{Fe} = 0.125$

We further investigate the *B*1-LS → *B*2-IS transition in *fp* with larger iron concentrations in $Fe_2Mg_{30}O$ and $Fe_4Mg_{28}O$ ($x_{Fe} = 0.0625$ and 0.125, noted as *fp*6 and *fp*12 hereafter). It has been shown that the iron arrangement in the *fp* solid solution has a minor effect on the spin state change pressure in the *B*1 phase, at least for small x_{Fe} as investigated here [48]. Therefore, we distribute Fe uniformly in both *B*1 and *B*2 lattices and disregard Fe-Fe interaction effects in the first order (see Supplemental Material Fig. S5 [44]). The relative enthalpies for different iron concentrations are shown in Fig. 4. With increasing iron concentration, the static *B*1-LS → *B*2-IS transition pressure increases from MgO to $(Fe_{0.125}Mg_{0.875})O$. PBE calculations show a systematically higher transition pres-
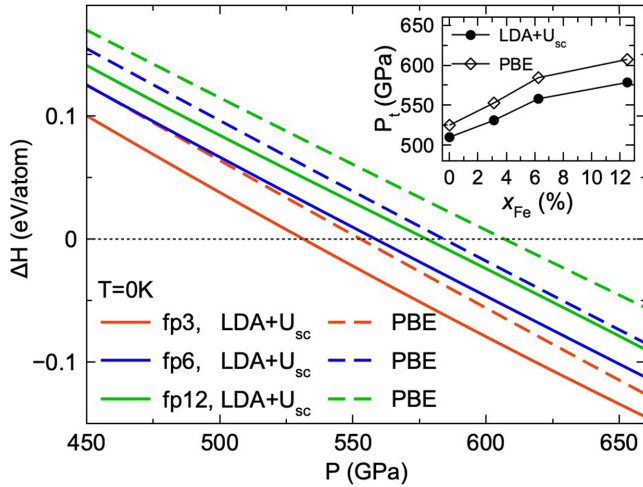
FIG. 4. Relative enthalpies between $B1$-low-spin (LS) to $B2$-intermediate-spin (IS) states in $fp3$, $fp6$, and $fp12$. The black dot line corresponds to the $B1$-LS state.

sure than the LDA $+ U_{sc}$ calculations, with a difference of 20–30 GPa. This difference is typical of what one expects from LDA and PBE calculations [47].

D. Thermodynamic phase boundary

We now compute the $B1$-LS $\rightarrow$ $B2$-IS thermodynamic phase boundary. We use the quasiharmonic approximation (QHA) to compute the vibrational free energy. Supplemental Material Figs. S3 and S4 [44] show phonon dispersions of the $B2$-IS phase using different functionals. It demonstrates that thermal electronic excitation with a high T_{el} is required to stabilize phonons in LDA $+ U_{sc}$ and PBE calculations. This stabilization is related to the stabilization of the metallic state. Electron-phonon interaction in the vibrating lattice might also decrease the gap and the required T_{el} for metallization. Phonon-phonon interaction might also help to stabilize the unstable modes. A dynamical mean-field theory calculation may be necessary to accurately address the effect of electron-electron interaction on the metallic state [28], and anharmonic phonon calculations should also elucidate these instabilities in the phonon spectrum.

Nevertheless, unavoidable thermal electronic excitations in LDA $+ U_{sc}$ calculations stabilize the metallic state and the phonon spectrum. If the phonon dispersion has no imaginary mode frequencies, the electronic temperature does not affect significantly the free enery, thermodynamic properties, and phase boundary [42]. We have tested the effect of electronic temperature on the phase boundary and found no significant difference between $T_{el} = 5000$ and 7000 K, as shown in Supplemental Material Fig. S8 [44]. Therefore, we chose to use a consistent $T_{el} = 7000$ K for all the phonon calculations shown in Fig. 5. This is an *ad hoc* choice but an approximation that enables a first glimpse of the stability field of these phases. Furthermore, with increasing pressure, phonon frequencies increase in both $B1$ and $B2$ phases. No imaginary frequency exists at these conditions. Therefore, at high temperatures, both $B2$-IS and $B1$-LS states of fp with $x_{Fe} < 0.125$ are dynamically stable in this calculation.

As recently pointed out [42], calculations of thermodynamic properties for metallic systems need to fully include thermal electronic excitation effects in a continuum of temperatures T_{el} in the static part of the calculation. The effect of T_{el} on the vibrational properties is more of a second-order effect, even though, here, we see it is crucial to stabilizing the $B2$-IS state. Despite this nonnegligible effect, once phonons stabilize, the impact of T_{el} on the vibrational free energy should be less significant than on the static energy. Here, we perform the static calculation in a T_{el} continuum. The electronic temperatures are sampled from 0 to 7000 K spaced by 1000 K with temperature interpolations. With the vibrational entropy S_{vib} from phonon dispersion, the Gibbs free energy of $B1$ and $B2$ phases can be computed using the QHA calculations. Obviously, $T_{el} = T$ when the system is in thermodynamic equilibrium. A common expression for the free energy in this case:

$$F(V, T, T_{el}) = F_{static}(V, T_{el}) + F_{vib}(V, T, T_{el}) - T S_{mag},$$
(2a)

where

$$F_{static}(V, T_{el}) = F_{Mermin}(V, T_{el})$$
(2b)

is the total Mermin free energy at volume V. Here,

$$F_{Mermin}(V, T_{el}) = E_{static}(V, T_{el}) - T_{el}S_{el}(V, T_{el}),$$
(2c)

where $E_{static}(V, T_{el})$ is the self-consistent energy with orbital occupancies:

$$f_{ki}(V, T_{el}) = \frac{1}{\exp\frac{\hbar(E_{ki} - E_F)}{k_B T_{el}} + 1},$$
(2d)

with E_{ki} being the one-electron energy of an orbital with wave number $\mathbf{k}$ and band index i, and E_F being the Fermi energy. The electronic entropy is

$$S_{el} = -k_B \sum_{\mathbf{k},i} [(1 - f_{ki})\ln(1 - f_{ki}) + f_{ki}\ln f_{ki}].$$
(2e)

The vibrational energy is

$$F_{vib}(V, T, T_{el}) = \frac{1}{2} \sum_{\mathbf{q},s} \hbar\omega_{\mathbf{q},s}(V, T_{el} = 0)$$
$$+ k_B T \sum_{\mathbf{q},s} \ln\left\{1 - \exp\left[-\frac{\hbar\omega_{\mathbf{q},s}(V, T_{el})}{k_B T}\right]\right\},$$
(2f)

where $\omega_{\mathbf{q},s}(V)$ is the vibrational frequency of noninteracting phonons with wave number $\mathbf{q}$ and polarization index s.

Another important contribution to free energy in fp is the magnetic entropy [26], here treated in the atomic impurity limit:

$$S_{mag} = k_B x_{Fe} n \ln[m(2S + 1)],$$
(2g)

where k_B is the Boltzmann constant, x_{Fe} is iron concentration, n is the fraction of $B2$-IS states, S is the iron total spin quantum number ($S = 0$ for LS and $S = 1$ for IS), and m is the orbital configuration multiplicity. For an insulating system, it is easier to count this multiplicity, and m
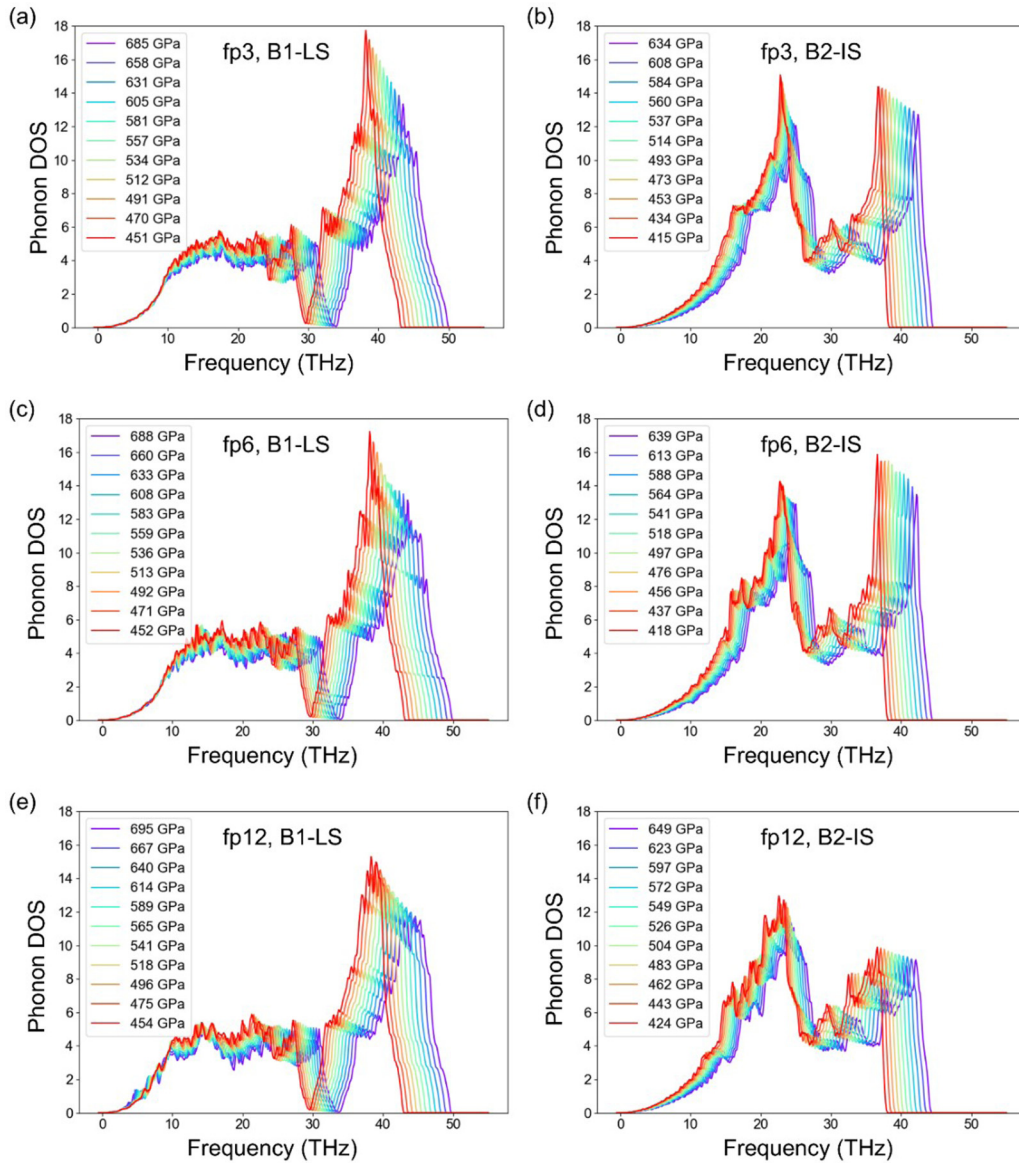
FIG. 5. Phonon density of states for (a) *B*1-low spin (LS) of *fp*3, (b) *B*2-intermediate spin (IS) of *fp*3, (c) *B*1-LS for *fp*6, (d) *B*2-IS of *fp*6, (e) *B*1-LS of *fp*12, and (f) *B*2-IS of *fp*12.

would be three if the *B*2-IS state were insulating. However, in a calculation with the Mermin functional, which includes electronic entropy, with nearly degenerate t_{2g} states at the Fermi level, it is more appropriate to define $m = 1$ for the *B*2-IS and LS states.

Next, we address the issue of configurational entropy. Here, *fp* is a solid solution of FeO and MgO. According to the Gibbs phase rule, this leads to a *B*1-*B*2 coexistence region [49]. Here, we use the QISS model to determine the co-existence region and phase boundary. This method, detailed in the Method section, only needs the free energy information for MgO and $(Fe_{0.125}Mg_{0.875})O$ and does not require the free energy data on the Fe-rich side [45]. We note that this method improves on the ISS model to compute the phase boundary for Mg-rich concentrations. As shown in the *B*1 phase, in Fe-rich concentrations, complex Fe-Fe interactions may lead to nonuniform iron distribution and symmetry reduction [50].

Figure 6 shows the pressure-concentration phase diagram for the $B1 \rightarrow B2$ transition at various temperatures. With increasing temperature, the phase boundary shifts to lower pressures. This is because the electronic entropy contributes more significantly to the stabilization of the *B*2 phase. More-over, as shown in Fig. 5, the *B*2 phase has smaller vibrational frequencies than the *B*1 phase due to larger bond lengths, resulting in larger vibrational entropy for this phase. There-fore, these entropic effects stabilize the *B*2 phase at higher temperatures. The *B*1-*B*2 coexistence region widens with in-creasing iron concentration, while it narrows down at higher temperatures. Results by LDA + U_{sc} and PBE are qualita-tively similar, except that the phase boundary by PBE is systematically shifted to higher pressures.

The *P*-*T* phase diagram for $x_{Fe} = 0.1$ is computed us-ing the QISS model and Eq. (1c) with both LDA + U_{sc} and PBE functionals. Because Eq. (2g) gives the maximum magnetic entropy in the metallic state, we also compute the
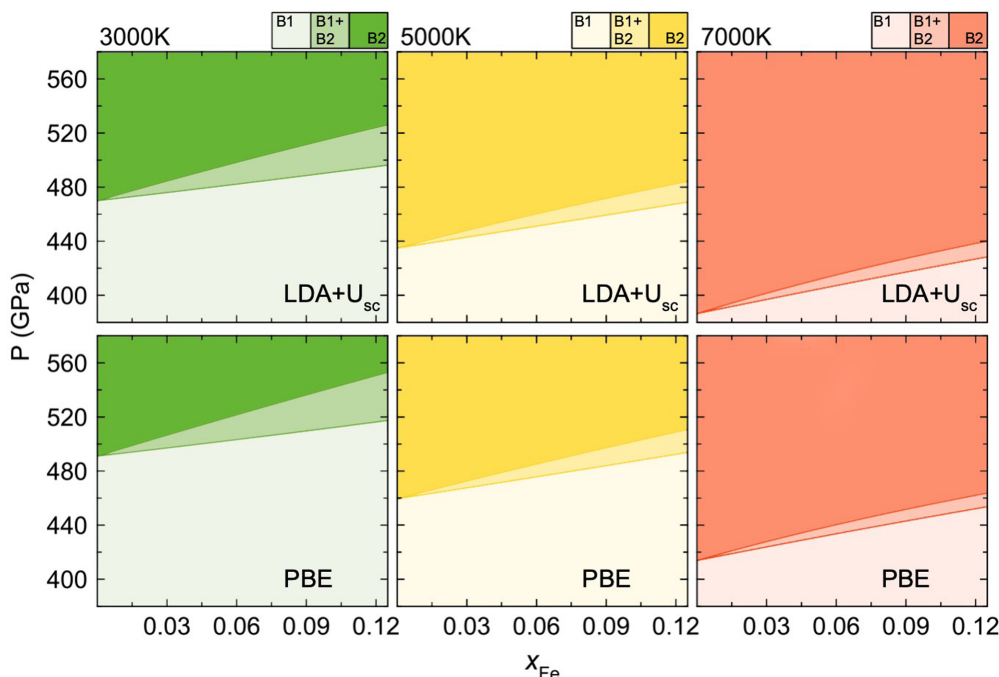
FIG. 6. Pressure-concentration phase diagram based on the quasi-ideal solid solution model.

phase diagram without this term, which provides the lower limit for S_{mag}. The phase boundaries with and without S_{mag} are shown in Fig. S7 in the Supplemental Material [44]. We find that S_{mag} does not significantly affect the phase boundary but changes the width of the coexistence region. Therefore, we provide the phase boundary in Fig. 7 using the average S_{mag}. The phase boundary shows a negative Clapeyron slope because entropic effects stabilize the $B2$ phase at high temperatures. This is consistent with the previous observations of large negative $B1$-$B2$ Clapeyron slope in both end members, FeO [51] and MgO [52]. Like static calculations, the high-temperature PBE calculations lead to a higher transition pressure of ~ 20 GPa compared with LDA $+ U_{\mathrm{sc}}$ calculations.

Upon further compression, we observe the $B2$-IS $\rightarrow B2$-LS state crossover. This spin-state change in the metallic system

can be addressed by inspecting the evolution of the average magnetic moment per iron. With a small electronic temperature of $T_{\mathrm{el}} = 1000$ K, we find the $B2$-IS state is dynamically stable up to 3.0 TPa. The pressure-dependent magnetization displayed in Fig. 8 shows no $B2$-IS $\rightarrow B2$-LS transition in static calculations for $T_{\mathrm{el}} = 1000$ K. Interestingly, with rising T_{el}, the average magnetic moment reduces more significantly with increasing pressure. At $T_{\mathrm{el}} = 5000$ K, the magnetic moment of $fp12$ in the $B2$ phase vanishes at $P = 2.75$ TPa in LDA $+ U_{\mathrm{sc}}$ calculations. The PBE calculation also identifies a similar IS $\rightarrow$ LS transition for $T_{\mathrm{el}} = 5000$ K at $P = 1.63$ TPa. Therefore, this spin-state change is much more sensitive to the functional than the $B1 \rightarrow B2$ structural transition. Moreover, comparing different conditions in Fig. 8, one can see that increasing T_{el} and x_{Fe} lower the $B2$-IS $\rightarrow B2$-LS transition pressure.
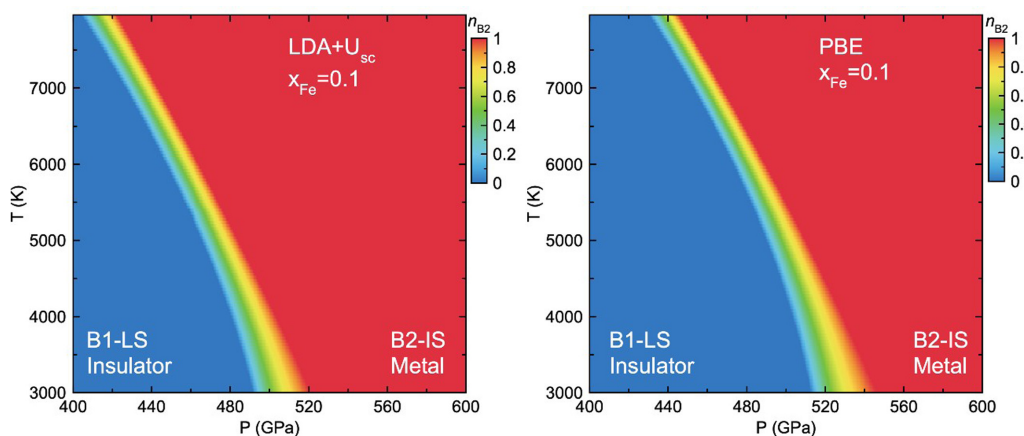

FIG. 7. Phase boundary between $B1$-low spin (LS) and $B2$-intermediate spin (IS) with $x_{\mathrm{Fe}} = 0.1$. The color bar shows nB_2, the molar fraction of the $B2$-IS phase; (a) LDA $+ U_{\mathrm{sc}}$ results; (b) PBE results. The $B2$-LS state plays an insignificant role in this phase transition.
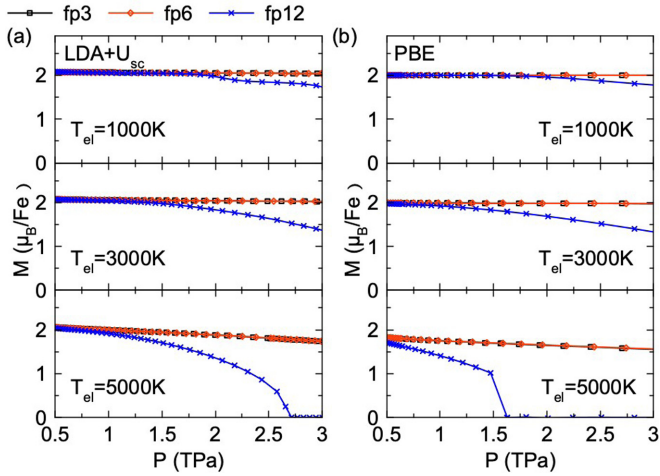
FIG. 8. Magnetic moment of iron vs pressure in $fp3$, $fp6$, and $fp12$ computed with (a) LDA + U_{sc} and (b) PBE. The temperatures for thermal electronic excitations T_{el} are indicated in each panel.

IV. DISCUSSION

These calculations in $B1$ and $B2$ phases suggest several states are possible for $Mg_{1-x}Fe_xO$ with $x_{Fe} \leqslant 0.125$. The ultrahigh pressure in super-Earths can lead to a complex, layered mantle structure. In the outer layers, one would expect $B1$-type fp. With increasing depth, fp first undergoes the HS-LS transition like that on Earth. Then fp transforms from the $B1$ to the $B2$ structure. The $B1$-$B2$ coexistence region spreads over a finite pressure range, e.g., $\sim\Delta25$ GPa at 3000 K. Along with the structural transition, the re-emergence of a magnetic state with a simultaneous IMT can have a strong impact on thermal and electrical conductivities, which will be important to model heat transport and convection in a multilayered super-Earth mantle. Coupling between the electromagnetic field produced in the core and the high magnetic induction of the metallic mantle could influence the temporal evolution of the magnetic field lines crossing the mantle. The metallization of the mantle could also affect the nutation of a super-Earth [53,54].

In this paper, we focus mainly on the solid solution with $x_{Fe} \leqslant 0.125$, which is relevant for fp. Because the $B1 \rightarrow B2$ transition pressure of FeO is lower than that of MgO but only exists >4000 K [51], the current trend of increasing transition pressure with increasing iron concentration should reverse at higher iron content. Iron-iron interactions may also cause the dissociation into a nonuniform solid solution, i.e., an iron-rich and an iron-poor phase separation in $x_{Fe} = 0.5$ [55]. Therefore, the phase transition at relevant higher iron concentrations needs a more robust thermodynamic treatment and is left for a future study.

While this paper was in preparation, a preprint [12] on the same topic became available. The authors of that study focus on the $B1 \rightarrow B2$ transition in fp with higher iron concentrations, e.g., $x_{Fe} = 0.125$ and 0.25. They used the LDA + U_{sc} functional as well. First, their static transition pressure decreases with increasing x_{Fe}, which we confirm. This is in line with the lower transition pressure of FeO than that in MgO recently found [10]. The increase in transition pressure we ob-

served for low x_{Fe} values suggests that fp becomes a non-ISS beyond $x_{Fe} = 0.125$. Second, their $fp12$ $B2$-IS phase displays a rhombohedral distortion, producing a semiconducting state with a small gap of 0.3 eV at $T_{el} = 0$ K. This result is qualitatively like ours on $fp3$ before considering the effect of thermal electronic excitations. Therefore, their rhombohedra phase should also become metallic at high temperatures and possibly also turn into a cubic phase. The LDA + U_{sc} calculation on the metallic state requires electronic entropic contributions to the internal energy using the Mermin functional [25]. Considering that thermal electronic excitations can stabilize phonons in the $B2$-IS state of the solid solution, our calculations with the cubic cell should be more appropriate to describe the $B1$-$B2$ high-temperature phase diagram.

The present calculation has explored the important effects of strong electronic correlation, thermal electronic excitations, structural distortions, and IMT on the phase stability of fp under pressure. However, given the complexity of the problem, it is likely that electron-phonon and phonon-phonon (anharmonicity) interactions still play important roles in the behavior of the MgO-FeO solid solution under pressure, more so at low temperatures. Experiments on fp with similar iron concentrations will be essential to help calibrate these challenging calculations.

V. CONCLUSIONS

In conclusion, *ab initio* calculations reveal a $B1$-to-$B2$ transition in fp accompanied by an IMT and the re-emergence of a local magnetic moment in iron corresponding to $S = 1$, the IS state. The stabilization of the IS state originates in the change in coordination from octahedral to cubic and the change in the energy level structure of the $3d$ electrons in Fe. Based on LDA + U_{sc} calculations, the $B1$-LS $\rightarrow$ $B2$-IS static transition pressure P_t varies from 526 GPa for $x_{Fe} = 0.03125$ to 576 GPa for $x_{Fe} = 0.125$. PBE calculations provide a similar trend, while the transition pressure is systematically higher by ~20–30 GPa. Phonon calculations confirm the dynamic stability of the $B2$-IS state in the currently studied pressure range. By including vibrational and electronic entropy contributions in the QISS model, we determine the $B1$-$B2$ phase boundary and the coexistence region up to 7000 K. The two-phase region widens with increasing iron concentration. The P-T phase diagram shows a negative Clapeyron slope. At ultrahigh pressure, the stability of the $B2$-IS state highly depends on the electronic temperature and iron concentrations. With increasing electronic temperature or iron concentration, the Fe magnetic moment tends to decrease to zero, the LS state. An IMT accompanies this $B1$-$B2$ phase change, and the iron magnetic moment re-emerges, which should have significant consequences for modeling the mantle structure and dynamics of a super-Earth. Although not considered in this paper, high-temperature anharmonic effects are likely to stabilize the $B2$ structure at lower temperatures. They will need to be included in future studies of the $B2$ structure. This will produce a more robust thermodynamic model for this transition in fp and will be indispensable to address higher iron concentrations x_{Fe}. For $x_{Fe} \geqslant 0.5$, the $B8$ phase might also have to be considered.

ACKNOWLEDGMENTS

[1] M. Akaogi and E. Ito, Refinement of enthalpy measurement of $MgSiO_3$ perovskite and negative pressure-temperature slopes for perovskite-forming reactions, Geophys. Res. Lett. **20**, 1839 (1993).

[2] A. E. Doyle, E. D. Young, B. Klein, B. Zuckerman, and H. E. Schlichting, Oxygen fugacities of extrasolar rocks: evidence for an Earth-like geochemistry of exoplanets, Science **366**, 356 (2019).

[3] K. Umemoto, R. M. Wentzcovitch, S. Wu, M. Ji, C. Z. Wang, and K. M. Ho, Phase transitions in $MgSiO_3$ post-perovskite in super-Earth mantles, Earth Planet. Sci. Lett. **478**, 40 (2017).

[4] A. P. van den Berg, D. A. Yuen, K. Umemoto, M. H. G. Jacobs, and R. M. Wentzcovitch, Mass-dependent dynamics of terrestrial exoplanets using *ab initio* mineral properties, Icarus **317**, 412 (2019).

[5] J. Badro, G. Fiquet, F. Guyot, J. P. Rueff, V. V. Struzhkin, G. Vankó, and G. Monaco, Iron partitioning in Earth's mantle: toward a deep lower mantle discontinuity, Science **300**, 789 (2003).

[6] R. E. Cohen, I. I. Mazin, and D. G. Isaak, Magnetic collapse in transition metal oxides at high pressure: implications for the Earth, Science **275**, 654 (1997).

[7] T. S. Duffy, R. J. Hemley, and H.-K. Mao, Equation of State and Shear Strength at Multimegabar Pressures: Magnesium Oxide to 227 GPa, Phys. Rev. Lett. **74**, 1371 (1995).

[8] K. Umemoto, R. M. Wentzcovitch, and P. B. Allen, Dissociation of $MgSiO_3$ in the cores of gas giants and terrestrial exoplanets, Science **311**, 983 (2006).

[9] F. Coppari, R. F. Smith, J. H. Eggert, J. Wang, J. R. Rygg, A. Lazicki, J. A. Hawreliak, G. W. Collins, and T. S. Duffy, Experimental evidence for a phase transition in magnesium oxide at exoplanet pressures, Nat. Geosci. **6**, 926 (2013).

[10] F. Coppari, R. F. Smith, J. Wang, M. Millot, D. Kim, J. R. Rygg, S. Hamel, J. H. Eggert, and T. S. Duffy, Implications of the iron oxide phase transition on the interiors of rocky exoplanets, Nat. Geosci. **14**, 121 (2021).

[11] S. Ritterbex, T. Harada, and T. Tsuchiya, Vacancies in MgO at ultrahigh pressure: about mantle rheology of super-Earths, Icarus **305**, 350 (2018).

[12] H. Hsu and K. Umemoto, Structural, spin, and metal-insulator transitions of (Mg,Fe)O at ultrahigh pressure, arXiv:2011.07737.

[13] F. Della Pia and D. Alfè, *B*1-*B*2 phase transition of ferropericlase at planetary interior conditions, Phys. Rev. B **105**, 134109 (2022).

[14] I. I. Mazin and V. I. Anisimov, Insulating gap in FeO: correlations and covalency, Phys. Rev. B **55**, 12822 (1997).

[15] M. Cococcioni and S. De Gironcoli, Linear response approach to the calculation of the effective interaction parameters in the LDA + U method, Phys. Rev. B **71**, 035105 (2005).

[16] A. Georges, G. Kotliar, W. Krauth, and M. J. Rozenberg, Dynamical mean-field theory of strongly correlated fermion systems and the limit of infinite dimensions, Rev. Mod. Phys. **68**, 13 (1996).

[17] N. Lanatà, T. H. Lee, Y. X. Yao, V. Stevanović, and V. Dobrosavljević, Connection between Mott physics and crystal structure in a series of transition metal binary compounds, npj Comput. Mater. **5**, 30 (2019).

[18] A. O. Shorikov, Z. V. Pchelkina, V. I. Anisimov, S. L. Skornyakov, and M. A. Korotin, Orbital-selective pressure-driven metal to insulator transition in FeO from dynamical mean-field theory, Phys. Rev. B **82**, 195101 (2010).

[19] V. I. Anisimov, J. Zaanen, and O. K. Andersen, Band theory and Mott insulators: Hubbard U instead of Stoner I, Phys. Rev. B **44**, 943 (1991).

[20] A. I. Liechtenstein, V. I. Anisimov, and J. Zaanen, Density-functional theory and strong interactions: orbital ordering in Mott-Hubbard insulators, Phys. Rev. B **52**, R5467 (1995).

[21] H. J. Kulik, M. Cococcioni, D. A. Scherlis, and N. Marzari, Density Functional Theory in Transition-Metal Chemistry: A Self-Consistent Hubbard U Approach, Phys. Rev. Lett. **97**, 103001 (2006).

[22] M. Cococcioni and N. Marzari, Energetics and cathode voltages of $LiMPO_4$ olivines (M = Fe, Mn) from extended Hubbard functionals, Phys. Rev. Materials **3**, 033801 (2019).

[23] A. Floris, I. Timrov, B. Himmetoglu, N. Marzari, S. de Gironcoli, and M. Cococcioni, Hubbard-corrected density functional perturbation theory with ultrasoft pseudopotentials, Phys. Rev. B **101**, 064305 (2020).

[24] H. Hsu, K. Umemoto, Z. Wu, and R. M. Wentzcovitch, Spin-state crossover of iron in lower-mantle minerals: results of DFT + U investigations, Rev. Mineral. Geochem. **71**, 169 (2010).

[25] Y. Sun, M. Cococcioni, and R. M. Wentzcovitch, LDA + U_{sc} calculations of phase relations in FeO, Phys. Rev. Materials **4**, 063605 (2020).

[26] T. Tsuchiya, R. M. Wentzcovitch, C. R. S. Da Silva, and S. De Gironcoli, Spin Transition in Magnesiowüstite in Earth's Lower Mantle, Phys. Rev. Lett. **96**, 198501 (2006).

[27] R. M. Wentzcovitch, J. F. Justo, Z. Wu, C. R. S. Da Silva, D. A. Yuen, and D. Kohlstedt, Anomalous compressibility of ferropericlase throughout the iron spin cross-over, Proc. Natl. Acad. Sci. USA **106**, 8447 (2009).

[28] E. Greenberg, R. Nazarov, A. Landa, J. Ying, R. Q. Hood, B. Hen, R. Jeanloz, V. B. Prakapenka, V. V. Struzhkin, G. K. Rozenberg, and I. Leonov, Phase transitions and spin-state of iron in FeO at the conditions of Earth's deep interior, arXiv:2004.00652 (2020).

[29] P. Giannozzi, O. Andreussi, T. Brumme, O. Bunau, M. Buongiorno Nardelli, M. Calandra, R. Car, C. Cavazzoni, D. Ceresoli, M. Cococcioni, N. Colonna, I. Carnimeo, A. Dal Corso, S. De Gironcoli, P. Delugas, R. A. Distasio,

A. Ferretti, A. Floris, G. Fratesi, G. Fugallo *et al.*, Advanced capabilities for materials modelling with QUANTUM ESPRESSO, J. Phys. Condens. Matter **29**, 465901 (2017).

[30] P. Giannozzi, S. Baroni, N. Bonini, M. Calandra, R. Car, C. Cavazzoni, D. Ceresoli, G. L. Chiarotti, M. Cococcioni, I. Dabo, A. Dal Corso, S. De Gironcoli, S. Fabris, G. Fratesi, R. Gebauer, U. Gerstmann, C. Gougoussis, A. Kokalj, M. Lazzeri, L. Martin-Samos *et al.*, QUANTUM ESPRESSO: a modular and open-source software project for quantum simulations of materials, J. Phys. Condens. Matter **21**, 395502 (2009).

[31] D. Vanderbilt, Soft self-consistent pseudopotentials in a generalized eigenvalue formalism, Phys. Rev. B **41**, 7892 (1990).

[32] K. Umemoto, R. M. Wentzcovitch, Y. G. Yu, and R. Requist, Spin transition in (Mg, Fe)SiO₃ perovskite under pressure, Earth Planet. Sci. Lett. **276**, 198 (2008).

[33] J. P. Perdew, K. Burke, and M. Ernzerhof, Generalized Gradient Approximation Made Simple, Phys. Rev. Lett. **77**, 3865 (1996).

[34] A. Dal Corso, Pseudopotentials periodic table: from H to Pu, Comput. Mater. Sci. **95**, 337 (2014).

[35] H. J. Monkhorst and J. D. Pack, Special points for Brillouin-zone integrations, Phys. Rev. B **13**, 5188 (1976).

[36] N. D. Mermin, Thermal properties of the inhomogeneous electron gas, Phys. Rev. **137**, A1441 (1965).

[37] R. M. Wentzcovitch, J. L. Martins, and P. B. Allen, Energy versus free-energy conservation in first-principles molecular dynamics, Phys. Rev. B **45**, 11372 (1992).

[38] I. Timrov, N. Marzari, and M. Cococcioni, Hubbard parameters from density-functional perturbation theory, Phys. Rev. B **98**, 085127 (2018).

[39] R. M. Wentzcovitch, Invariant molecular-dynamics approach to structural phase transitions, Phys. Rev. B **44**, 2358 (1991).

[40] R. M. Wentzcovitch, J. L. Martins, and G. D. Price, *Ab Initio* Molecular Dynamics with Variable Cell Shape: Application to MgSiO₃, Phys. Rev. Lett. **70**, 3947 (1993).

[41] A. Togo and I. Tanaka, First principles phonon calculations in materials science, Scr. Mater. **108**, 1 (2015).

[42] J. Zhuang, H. Wang, Q. Zhang, and R. M. Wentzcovitch, Thermodynamic properties of ε-Fe with thermal electronic excitation effects on vibrational spectra, Phys. Rev. B **103**, 144102 (2021).

[43] D. C. Wallace and H. Callen, Thermodynamics of crystals, Am. J. Phys. **40**, 1718 (1972).

[44] See Supplemental Material at https://link.aps.org/supplemental/10.1103/PhysRevResearch.4.023078 for detailed explanation of quasi-ideal solid solution model, projected density of states and phonon dispersions, atomic structure of supercells, phase boundary, and equation of state parameters.

[45] J. Zhuang, J. Valencia-Cardona, R. Wentzcovitch, G. Shukla, and Kanchan Sarkar, The post-perovskite transition in Fe- and Al-bearing bridgmanite: effects on seismic observables, in *Bulletin of the American Physical Society* (American Physical Society, 2022)

[46] H. Hsu and R. M. Wentzcovitch, First-principles study of intermediate-spin ferrous iron in the Earth's lower mantle, Phys. Rev. B **90**, 195205 (2014).

[47] R. M. Wentzcovitch, Y. G. Yu, and Z. Wu, Thermodynamic properties and phase relations in mantle minerals investigated by first principles quasiharmonic theory, Rev. Mineral. Geochem. **71**, 59 (2010).

[48] M. L. Marcondes, F. Zheng, and R. M. Wentzcovitch, Phonon dispersion throughout the iron spin crossover in ferropericlase, Phys. Rev. B **102**, 104112 (2020).

[49] D. R. Gaskell, *Introduction to the Thermodynamics of Materials* (CRC Press, New York, 2008).

[50] Y. Fei, L. Zhang, A. Corgne, H. Watson, A. Ricolleau, Y. Meng, and V. Prakapenka, Spin transition and equations of state of (Mg, Fe)O solid solutions, Geophys. Res. Lett. **34**, L17307 (2007).

[51] H. Ozawa, F. Takahashi, K. Hirose, Y. Ohishi, and N. Hirao, Phase transition of FeO and stratification in Earth's outer core, Science **334**, 792 (2011).

[52] D. Cebulla and R. Redmer, *Ab initio* simulations of MgO under extreme conditions, Phys. Rev. B **89**, 134107 (2014).

[53] B. A. Buffett, E. J. Garnero, and R. Jeanloz, Sediments at the top of Earth's core, Science **290**, 1338 (2000).

[54] B. A. Buffett, Constraints on magnetic energy and mantle conductivity from the forced nutations of the Earth, J. Geophys. Res. **97**, 19581 (1992).

[55] L. S. Dubrovinsky, N. A. Dubrovinskaia, S. K. Saxena, H. Annersten, E. Halenius, H. Harryson, F. Tutti, S. Rekhi, and T. Le Bihan, Stability of ferropericlase in the lower mantle, Science **289**, 430 (2000).